Energy from Garbage: Recycling Heavy Metal-Containing Wastewater Adsorbents for Energy Storage

ADVANCED ENERGY & SUSTAINABILITY RESEARCH
www.advenergysustres.com

Energy from Garbage: Recycling Heavy Metal-Containing Wastewater Adsorbents for Energy Storage

*Marcelo A. Andrade, Olivier Crosnier, Patrik Johansson, and Thierry Brousse**

The global challenge of heavy metal contamination in wastewater necessitates efficient adsorbents, which, while they can effectively remove contaminants, ultimately become toxic waste themselves. Recycling wastewater adsorbents loaded with heavy metals is an alternative to their disposal as toxic garbage. This study presents a genuine recycling strategy for heavy metal-loaded adsorbents, repurposing them as electrode materials for energy storage applications, that is, electrochemical capacitors, and thus synergistically tackles water purification and waste valorization. Graphene oxide was prepared via the improved Hummers' method, and subsequently, a reduced graphene oxide (rGO) foam was hydrothermally synthesized. This rGO-based foam adsorbed >95% of the Hg^{2+} ions in a 100 ppm solution, using a dose = 500 mg L^{-1}, and up to 240 mg of Hg^{2+} ions/g on average at 25 °C, which are among the highest values reported so far. Electrochemically, the Hg-loaded rGO (rGO/Hg_{ads}) exhibits mercury redox activity and a 15% increase in capacity as compared to pristine rGO in an aqueous cell. Overall, this demonstrates the potential of reprocessed wastewater adsorbents as efficient and sustainable electrodes for high-power energy storage (time constant $\tau = 11$ s), offering a compelling solution to add more value and extend the life cycle of waste materials.

1. Introduction

The presence of heavy metals in wastewater is a major environmental concern. The terminology heavy metal normally refers to metallic elements with atomic numbers higher than 20 that can be toxic even in small doses.[1] Their accumulation in water bodies can have significant implications for human health as well as for the environment, coming from various sources, including industrial effluents, agricultural runoff, and mining activities.[2]

The problem of heavy metal pollution in wastewater is particularly critical in developing countries, where industrial regulation is often weaker and wastewater treatment facilities are inadequate. Mercury is a particularly problematic heavy metal from which human exposure can have various adverse health effects, including neurological damage, kidney failure, and reproductive problems.[3,4] It can enter wastewater and flow into rivers and streams, where it can bioaccumulate in fish and other aquatic life. Typically, this comes from illegal mining activities. Mercury is used in the artisanal and small-scale gold mining (ASGM) sector to extract gold from ore by forming an amalgam, which is then heated to vaporize the mercury, leaving behind the gold. According to the United Nations Environment Programme, an estimated 1220 tons of mercury are released yearly from ASGM activities, more than twice the amount released to water by other sources.[5]

Furthermore, besides the critical environmental problem, mercury pollution can significantly impact wastewater treatment plants. Mercury can bind to the active sites of enzymes in bacteria, disrupting the biological processes widely used to treat wastewater. This can lead to reduced treatment efficiency and the release of untreated or partially treated wastewater into the environment.[6,7] Wastewater treatment plants, hence, need to remove mercury using different technologies, such as adsorption, ion exchange, and reverse osmosis.[2,8,9]

Physical adsorbents typically have a high affinity for heavy metal cations and are already widely used in wastewater treatment.[10] Carbon-based adsorbents are among the most

M. A. Andrade, O. Crosnier, T. Brousse
CNRS
Institut des Matériaux de Nantes Jean Rouxel
IMN
Nantes Université
2 Rue de la Houssinière, 44322 Nantes, France
E-mail: thierry.brousse@univ-nantes.fr

The ORCID identification number(s) for the author(s) of this article can be found under https://doi.org/10.1002/aesr.202400195.

DOI: 10.1002/aesr.202400195

M. A. Andrade, O. Crosnier, T. Brousse
Réseau sur le Stockage Electrochimique de l'Energie (RS2E)
FR CNRS 3459, Hub de l'Energie, 15 Rue Baudelocque, 80039 Amiens, France

M. A. Andrade, P. Johansson
Alistore-ERI European Research Institute
FR CNRS 3104, Hub de l'Energie, 15 Rue Baudelocque, 80039 Amiens, France

P. Johansson
Department of Physics
Chalmers University of Technology
SE-412 96 Gothenburg, Sweden

popular solutions, given their low price, high availability, high affinity for waste adsorption, and large surface area.[11,12] A proposed adsorbent for heavy metal removal is reduced graphene oxide (rGO)-based foams,[13–18] which present high surface areas and pore volumes, which gives them a high adsorption capacity. Once the rGO foam has reached its maximal adsorption capacity, it can be regenerated a few times, but eventually, it becomes a toxic waste itself.[19] Recycling adsorbents loaded with heavy metal cations is one possible approach to reduce the environmental impact of heavy metal removal/disposal.[20–22]

In the literature, Godiya et al. repurposed a carboxymethyl cellulose (CMC) and polyacrylamide (PAM) hydrogel used to adsorb Cu^{2+}, Pb^{2+}, and Cd^{2+} ions. Their spent Cu-loaded CMC/PAM hydrogel adsorbents were used for rapid and efficient electrochemical reduction of toxic 4-nitrophenol to 4-aminophenol.[23] A second example is incorporating spent adsorbents into ceramic materials. Verbinnen et al. mixed zeolite or perlite-supported iron-based adsorbents loaded with heavy metals such as molybdenum (Mo) and others (Cr, Ni, Cu, Zn, As, Cd, Pb) with industrial sludge, followed by heating to 1100 °C. This process effectively reduced the leaching concentrations of these contaminants, stabilizing them within the ceramic matrix.[24] However, by far, most of the proposed recycled absorbents are electronically insulating or poorly conductive, which limits their reuse in electrochemical applications.

One innovative recycling solution, aiming at our society's environmental and energetic demands, would be repurposing the heavy metal-loaded adsorbents as active materials in energy storage devices. Electrode materials for electrochemical capacitors, for instance, must have high surface areas and good electrical conductivities—exactly what rGO foams offer, and they have previously been successfully used as performant electrode materials for electrochemical double-layer capacitors (EDLCs).[25,26]

The transformation of waste materials into suitable active materials for supercapacitor application is indeed an evolving area of interest in general.[27,28] Lei et al. developed a porous N-doped banana flesh-derived carbon aerogel, through a straightforward process of carbonization and CO_2 activation. The aerogel was then used in the fabrication of a supercapacitor, rendering a high specific capacitance of 178.9 F g^{-1} at 1 A g^{-1} from this low-cost raw material and simple synthesis method.[29]

The use of wastewater absorbents specifically in energy storage is, however, not yet widely explored. The limited research available suggests that specific modifications are needed before they can be effectively repurposed.[30,31] Wang et al. demonstrated the reuse of nickel-loaded biochar sorbents derived from dairy manure and sewage sludge. After undergoing microwave treatments, these were used in supercapacitors, which showed a doubled specific capacitance as compared to the original biochar-based supercapacitors. This was primarily attributed to the conversion of nickel into NiO and NiOOH. The specific capacitance was maintained at >98% of the initial value after 1000 charge-discharge cycles.[32] However, the recovered residues must be highly processed and undergo high-temperature treatments before being used as adsorbents, as well as an activation process using high-power microwave treatment to be used as energy storage device electrodes.

Here, we demonstrate a novel, straightforward approach for recycling wastewater adsorbents by *directly* repurposing them as electrode materials for EDLCs, as schematically detailed in **Figure 1**. An rGO foam was synthesized using a single-step hydrothermal treatment and subsequently used as an adsorbent for Hg^{2+} cations. Then, the Hg-loaded rGO foam (rGO/Hg_{ads}) was repurposed as an electrode for an electrochemical capacitor. Combined, we demonstrate the potential of recycled wastewater adsorbents as efficient and sustainable electrodes for high-power energy storage devices by both emphasizing the potential of such materials, then practically creating the adsorbent and using it to adsorb heavy metals, performing extensive characterization of the pristine and spent adsorbents, and finally evaluating their electrochemical performance using different protocols and measures.

2. Results and Discussion

2.1. Basic Considerations

2.1.1. Design Criteria

Choosing suitable adsorbents requires to consider several criteria: cost, density, availability, adsorption capacity and selectivity, etc. When the final goal is to use the adsorbents as active materials in supercapacitors, other intrinsic properties must also have

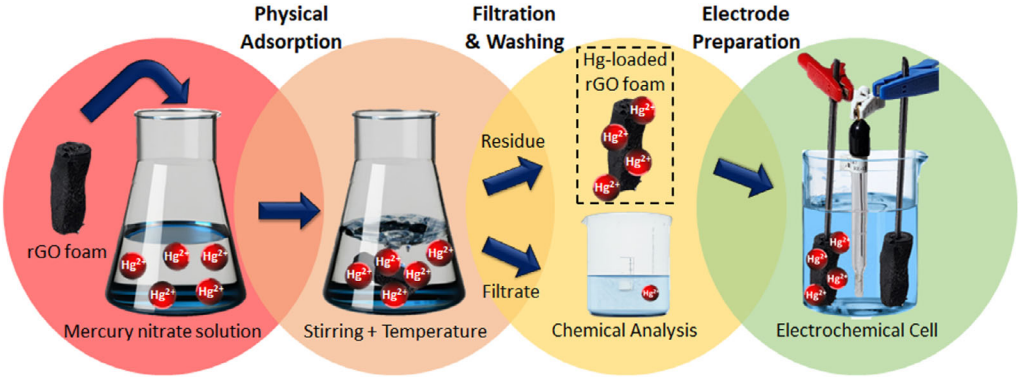

Figure 1. General scheme of the straightforward use of an adsorbent for mercury depollution and subsequent repurposing as an electrode for an energy storage device.

priority. The material's specific surface area (SSA), porosity, and conductivity must all be considered. Hence, the best adsorbents here are those fulfilling the combined requirements optimally.

Literature reports must be carefully and critically analyzed before choosing an adsorbent. The adsorption capacity normalization, for instance, can give a false impression of a very high total metal content after adsorption if it uses the mass of active adsorbent material rather than the total adsorbent mass.[33] The most critical property for repurposing is the latter, as it is the content of metals that will contribute to the electrode's final capacity, without further purification or concentration.

Here, we have chosen a porous rGO foam as our proof-of-concept platform. rGO foams are known to present good electrical conductivity and capacitance,[26] besides being easy to synthesize and have relatively low cost, high surface area, low density, and finally, very good heavy metal adsorption capacity.[34] In order to estimate the capacity improvement of the electrode, a few assumptions have been made: a constant specific capacitance over the whole potential window and that all adsorbed cations undergo redox half-reactions, such as indicated in Reaction (1), and thus contribute with 100% efficiency to the total capacity. Calculations based on these assumptions and this reaction (SI_2) were used to estimate the possible different charge storage contributions as a function of the amount of adsorbed cations in the rGO foam (M%, wt.)

$$M^{x+} + ne^- \rightarrow M^{(x-n)} \quad (1)$$

2.1.2. Capacity Estimation

Initially, the electrode of mass m_T (g) is considered to be composed of certain weight percentages of active material (A%), binder (B%), and conductive additive (C%). The usually reported capacity value in the literature is the active material capacity (Q_{AM}, C g^{-1}), obtained by normalizing the total electrode capacity (q_t, C) by $A\%.m_T$, as shown in Equation (2). In practice, the electrode capacity is obtained by the integration of the discharge current (I, A) over time (t, s) and can be described by two main contributions, as indicated in Equation (3): q_{redox}, coming from the faradaic processes involving the adsorbed cations, and q_{EDLC}, which is the non-faradaic contribution to the energy storage, coming from the electrochemical double-layer formation on the carbon surface

$$Q_{AM} = \frac{q_t}{A\%.m_T} \quad (2)$$

$$q_{total} = \int_0^t I_{(t)} \times dt = q_{redox} + q_{EDLC} \quad (3)$$

q_{redox} is directly dependent on the number of electrons (n) transferred in the half-reaction (Reaction (1)), as well as the Faraday constant (F), and inversely proportional to the molecular weight (M_w) of the adsorbed element (Equation (4)). Hence, the lighter the metal and the higher its oxidation state, the larger its contribution to q_{redox}. It also depends on the mass of metal in the electrode (m_M, g)

$$q_{redox} = m_M \frac{nF}{M_w} \quad (4)$$

In a cyclic voltammetry experiment, the obtained current (I_{EDLC}) is dependent on the scan rate (dV/dt), with an ideally constant capacitance (**C**). Using the first level approximation that the capacitance will not change with the scan rate and that the scan rate (or discharging current) is constant, the derivatives can be considered as a potential difference (ΔV) within the duration of one whole cycle (Δt). Equation (5) expresses these consequences, arriving at the q_{EDLC} contribution, which shows a direct dependency on the capacitance of the electrode (**C**, F)

$$q_{EDLC} = C \times \Delta V \quad (5)$$

Finally, the active material, binder, and conductive additive are considered to be contributing to C proportionally to their mass content m_a, m_b, and m_c, respectively, according to Equation (6). The capacitance contribution of the metal on the active material is negligible, so this term can be expressed as a function of the capacitance of the carbon foam (C_{rGO}, F g^{-1}) and its mass (m_{rGO}, g)

$$C = m_{rGO}C_{rGO} + m_bC_{binder} + m_cC_{conductive\ additive} \quad (6)$$

Here, the chosen electrode composition was $A = 70\%$, $B = 10\%$, and $C = 20\%$, with C_{binder} considered to be equal to zero, thus treated as dead weight, while for other parameters, the details are summarized in Table S1, Supporting Information. It is important to note that what is here called "specific capacity" refers to Q_{AM} (C g^{-1}), obtained by normalizing the electrode capacity q_{total} by the contribution of *active material* according to Equation (2). This value slightly overestimates the actual active material capacity by neglecting the *binder* and *conductive agent* contributions, which account for a capacity that is not coming from the active material.

Examples for Cr^{6+} and Cu^{2+} cations (Figure S1, Supporting Information) and charge contributions of Cr^{6+}, Cu^{2+}, Fe^{3+}, Hg^{2+}, and Pb^{2+} cations (Figure S2, Supporting Information) outline the general prospects, while the calculated maximum adsorption of Hg^{2+} cations in the rGO foam (**Figure 2**) provides the more concrete picture.

The major finding is that even at contents as low as 10 wt% of Hg^{2+} cations in the active material, the increase in the total charge storage capacity of the electrode can be >30%.[35]

2.2. Characterization

2.2.1. Mercury (II) Adsorption

The adsorption of Hg^{2+} cations was performed both at 25 and 60 °C using a simple physical adsorption procedure at equilibrium time (t_{eq}; min), and the uptake per unit mass of rGO foam (q_{eq}; mg g^{-1}) was calculated as the difference between the initial (C_0; mg L^{-1} ≈ppm) and the equilibrium (C_e; mg L^{-1} ≈ppm) concentrations, normalized by the dose of adsorbent (d; mg L^{-1}) (Equation (7))

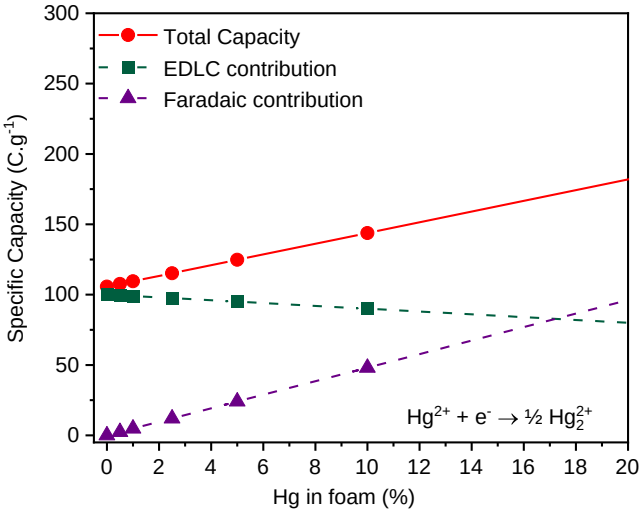

Figure 2. Theoretical capacity (in C g^{-1}) of an electrochemical capacitor using a capacitive material with capacitance = 100 F g^{-1} within a voltage window of 1.0 V. The contribution of mercury ions undergoing the half-reaction shown in the right-bottom corner increases with the heavy metal cation concentration (purple triangles, dashed line) as does the total capacity (red circles, solid line), while the capacitive (non-faradaic) contribution decreases (green squares, dashed line).

$$q_{eq} = \frac{(C_0 - C_{eq})}{d}; \quad \text{where} \quad d = \frac{m_{adsorbent}}{V_{solution}} \tag{7}$$

The mercury adsorption capacities at 25 °C (298 K) and 60 °C (333 K) as functions of the dose (a and b) and the pH (c and d) are reported in **Figure 3**.

Mercury can apparently be efficiently removed from standard solutions by the rGO foam at both temperatures; the 240 ± 15 mg g^{-1} at 25 °C (Figure 3a) is among the highest reported uptakes for this type of material,[10,15,16,18] which further increases to 300 ± 30 mg g^{-1} at 60 °C (Figure 3b), and by this, the standard solution is almost entirely depleted on mercury. Using a 500 mg L^{-1} dose of foam at 60 °C, the remaining concentration is <5 ppm, which is beyond the detection limit, making it impossible to obtain the average uptake capacity.

The cation uptake capacity increases proportionally with the pH, reaching a maximum of 245 ± 5 mg g^{-1} at pH = 5 (Figure 3c,d). As described in the literature,[36] a low pH, that is, a high concentration of H_3O^+, can hinder metal cation adsorption by competition of sites. Therefore, increasing the pH favors the adsorption of Hg^{2+} cations, but only until the point where $HgO_{(s)}$ starts to precipitate (around pH = 7).[37] Hence, to avoid precipitation and maximize the mercury adsorption content, pH = 5 was chosen, and the recovered rGO/Hg_{ads} adsorbents selected for further electrochemical studies were those used at 60 °C.

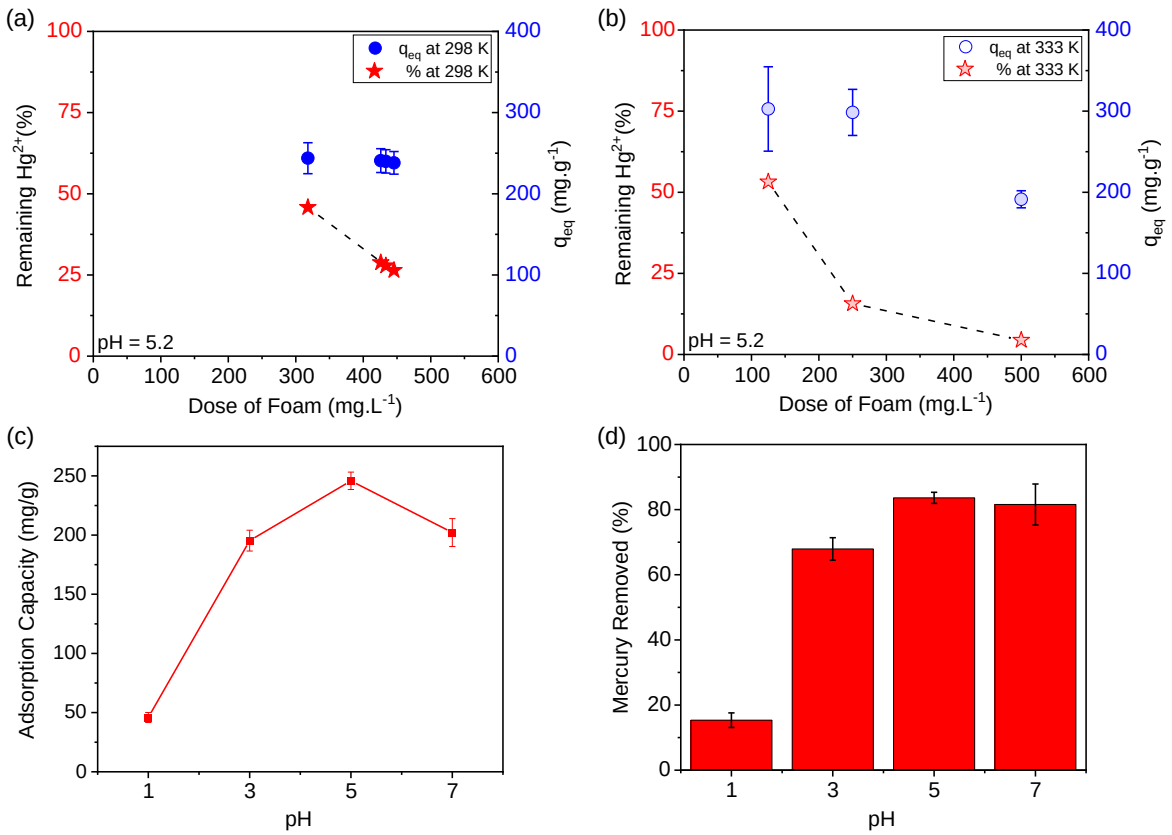

Figure 3. a) Adsorption of mercury with increasing dose of foam at $T = 298$ K, $C_0 = 150$ ppm, $t_{eq} = 150$ min (filled pattern) and b) at $T = 333$ K, $C_0 = 100$ ppm, $t_{eq} = 150$ min (transparent pattern). Remaining mercury ions in solution (red) and specific equilibrium capacity (q_{eq}) of the material (blue). c) Hg^{+2} cations removal and d) q_{eq} as a function of pH, varying from from 1 to 7. $C_0 = 150$ ppm, $d = 500$ mg L^{-1}, $T = 298$ K, $t_{eq} = 150$ min.

Comparatively, the adsorption of chromium (III) and bismuth (III) cations (at 25 °C) is considerably lower (Figure S3, Supporting Information), and these weaker interactions can be explained by the hard and soft Lewis acids and bases theory, given that a harder acid, such as the Cr^{3+} cation, would interact better with a hard base, such as a hydroxide group, which are not abundantly present in the rGO foam. In contrast, Hg^{2+} cations, being soft acids, interact efficiently with the soft electron clouds of the rGO foam graphene aromatic rings. Furthermore, Pb^{2+} cations are considered intermediate/soft acids and Bi^{3+} cations as intermediate/hard acids, which thus explains the trend: $q_{Cr} < q_{Bi} < q_{Pb} < q_{Hg}$.[38]

2.2.2. Morphological Characterization

The rGO foam was characterized before and after mercury adsorption, as well as its graphene oxide (GO) precursor. Gas adsorption experiments (BET) were conducted *via* adsorption isotherms to assess the SSAs and the pore size distributions of GO, rGO, and rGO/Hg_{ads} (Figure S4, Supporting Information). The largest SSA was obtained for the rGO foam before mercury adsorption, up to 214 $m^2 g^{-1}$, with an average pore size of 5.4 nm diameter, in agreement with the literature for similar materials.[14,39] After mercury adsorption, however, the SSA decreased to *ca.* ¼: 51 $m^2 g^{-1}$, which most probably is a consequence of the closing of smaller pores upon drying, as the new average pore size increased to 7.5 nm, indicating loss of small pores.

Looking at the materials' surfaces, scanning electron microscopy (SEM) of the GO (Figure S5, Supporting Information) highlights the formation of aggregated layers of a 2D, poorly conductive material (bright zones indicate charge accumulation occurring at the edges of graphene sheets). Some GO sheets can be seen on the edges of the aggregates, confirming the 2D character of the material and the proper exfoliation from the graphite precursor. After hydrothermal reduction, the GO sheets are rearranged into a porous 3D structure, forming the self-standing rGO foam. Using a lower magnification (**Figure 4**a), the overall highly porous branched morphology with low density of the rGO foam is visualized, while the 2D morphology and arrangement of the graphene sheets are revealed in more detail using a higher magnification (Figure 4b), including stacking of several graphene layers as well as exposed rGO edges. The lyophilized rGO foam after mercury adsorption exhibits a very similar structure (Figure 4c), indicating no major effect on either the shape or the size of the pores.

Moving to transmission electronic microscopy (TEM) images, obtained using scanning mode at 80 kV beam voltage in order to provide the highest resolution without damaging the GO, rGO, and rGO/Hg_{ads} samples, the lowest magnification images (Figure S6, Supporting Information) mainly confirm the SEM microstructures: GO sheets in Figure S6a, Supporting Information and the rGO foam microstructure in Figure S6b and S6c, Supporting Information. Furthermore, the TEM images reveal a highly isomorphic nature and intricate 3D configuration of the rGO as well as verify, at lower magnifications, that both rGO and rGO/Hg_{ads} foams possess the same general morphology.

With increasing the magnification to 2.3 Mx, and due to the (very) high contrast given by the large atomic weight difference between carbon and mercury, it is possible to distinguish shiny white dots with a 300 pm average diameter, which we assign to mercury cations adsorbed at the surface of and in the bulk of the foam (**Figure 5**). To the best of our knowledge, this is the first time ever that this kind of evidence of adsorbed cations at the surface of a lighter adsorbent is reported. A more powerful TEM microscope with temperature control and lower beam voltage could allow even better magnification and enable to locate the adsorbed cations within the carbon structure more accurately.

2.2.3. Chemical Characterization

The effective reduction of GO to rGO was confirmed by energy-dispersive spectroscopy (EDS) data (Figure S7, Supporting Information) primarily by a 24% decrease in oxygen content from GO to rGO (**Table 1**). The same 24% decrease in oxygen content was evidenced by electron energy loss spectroscopy (EELS) data (Figure S8, Supporting Information), which further confirms the effective reduction. For both techniques, the oxygen-to-carbon ratio was found the same for rGO and rGO/Hg_{ads}.

The EDS analysis also revealed the presence of small quantities of sulfur (<2% at.), which are traces from the use of sulfuric acid in the GO synthesis, but these are washed away after reduction to rGO. The mercury content was on average 1% at. and 16% wt., with significantly higher values for the most porous regions, indicating a nonhomogeneous mercury distribution.

X-ray photoelectron spectroscopy (XPS) for binding energies ranging from 0 to 1200 eV shows two prominent peaks

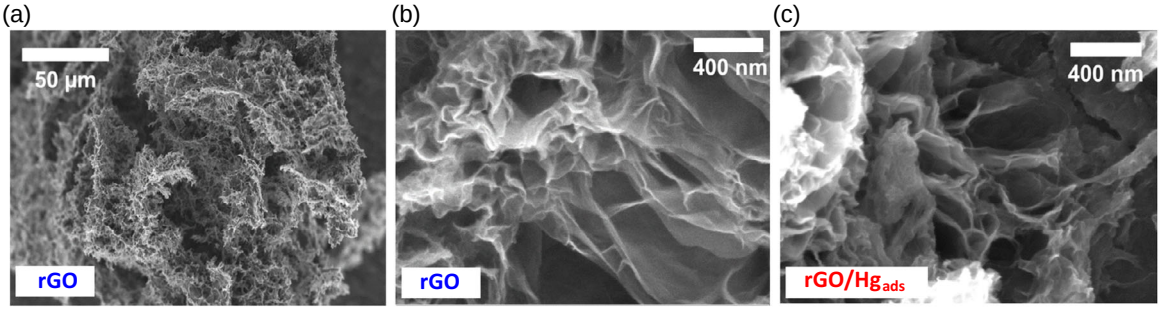

Figure 4. a,b) SEM images of the pure rGO and c) rGO/Hg_{ads}.

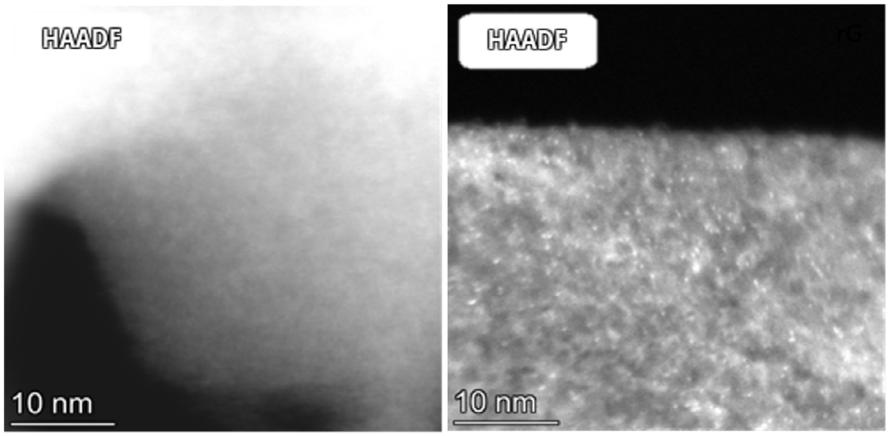

Figure 5. High resolution scanning/transmission electronic microscopy (HRSTEM) images of rGO (left) and rGO/Hg_{ads} (right).

Table 1. Elemental composition determined with different analytical techniques.

	Element	EDS		EELS	XPS		TGA
		Atomic [%]	Weight [%]	Atomic [%]	Atomic [%]	Weight [%]	Weight [%]
GO	C	61 ± 2	54 ± 2	75 ± 3	–	–	–
	O	37 ± 3	42 ± 3	25 ± 1	–	–	–
	S	2 ± 1	4 ± 1	–	–	–	–
rGO	C	72 ± 4	65 ± 4	80 ± 3	84.5	80	–
	O	28 ± 4	35 ± 4	19 ± 1	15.5	20	–
rGO/Hg_{ads}	C	72 ± 2	58 ± 2	84 ± 4	82.8	72.7	–
	O	27 ± 2	26 ± 2	16 ± 1	15.6	18.3	–
	Hg	1.2 ± 0.1	16.2 ± 0.3	–	0.6	9	16

associated with O 1*s* and C 1*s* and distinctly no other elements for rGO (**Figure 6**). The small peak at around 980 eV is related to the O KLL emission, an energy of electrons ejected after the filling of the O K shell by L shell electrons coupled with the ejection of an L shell electron.[40] The spectrum of rGO/Hg_{ads} is very similar: the presence of the O 1*s*, C 1*s*, and O KLL peaks. However, two new peaks can also be observed: one is associated with Hg 4*f* at 101 eV (Hg $4f_{7/2}$) and 105 eV (Hg $4f_{5/2}$) and the second with Hg 4*d* at 360 eV (Hg $4d_{5/2}$) and 380 eV (Hg $4d_{3/2}$). The absence of other elements, such as nitrogen from NO_3^- groups, is evidence for proper adsorption of Hg^{2+} cations and effective washing to remove the nitrate salt, as XPS is a very sensitive surface technique.

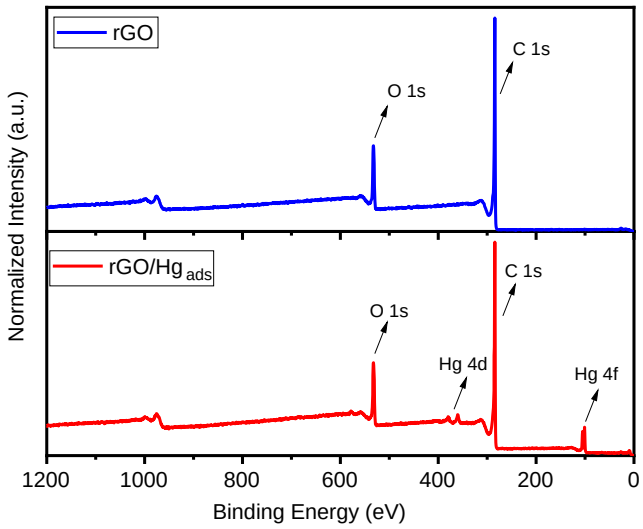

Figure 6. Survey XPS spectra of the pure rGO (top, blue) and rGO/Hg_{ads} (bottom, red) evidencing the presence of mercury.

The carbon, oxygen, and mercury peaks were further studied using XPS high-resolution spectra. Peak deconvolution enabled to determine the precise positions of the Hg $4f_{7/2}$ at 101.1 eV and the Hg $4f_{5/2}$ at 105.2 eV (Figure S9, Supporting Information). The fact that these energies are shifted as compared to metallic mercury[41] can be an indication of the mercury being present in a carbon-oxygen environment, such as oxalate (Hg $4f_{7/2}$ at 101.1 eV) or HgO,[42] but the chemical environment of mercury cannot be unambiguously determined based only on this spectrum. Furthermore, the carbon 1*s* peaks were deconvoluted for both rGO and rGO/Hg_{ads} (**Figure 7**, **Table 2**), and here we find that the presence of mercury does not induce any appearance of new peaks or substantial changes in the carbon-oxygen bonding contributions.

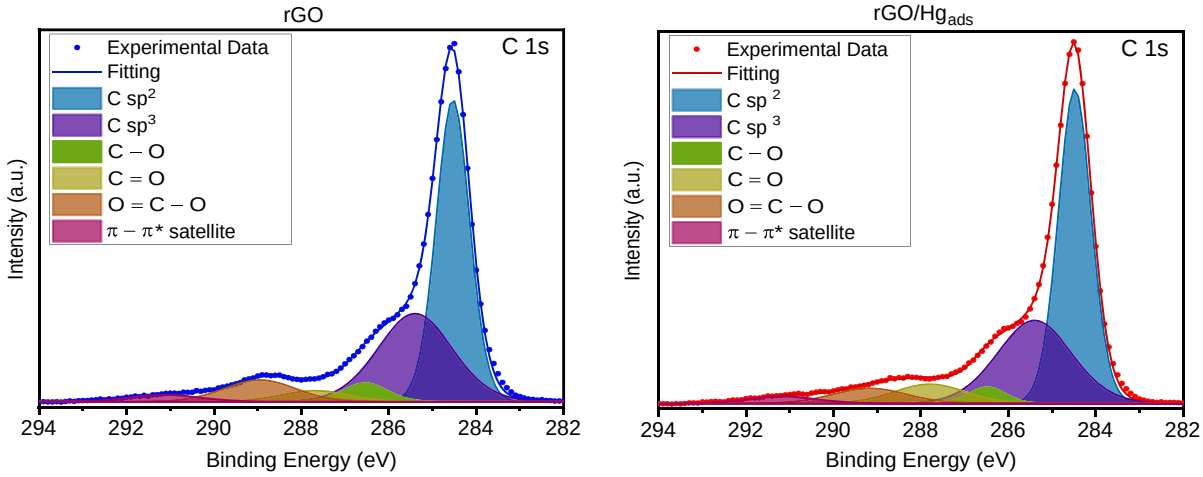

Figure 7. Carbon 1*s* XPS peaks' deconvolution for the rGO (left) and rGO/Hg_{ads} (right) samples.

The spectra similarity can be tentatively explained by two main factors: mercury concentration and physical adsorption. First, the low concentration of mercury atoms in rGO/Hg_{ads} (1% at.) might not be sufficient to induce a significant/observable change in the carbon chemical environment. Second, the possibly purely electrostatic interactions between the mercury cations and the carbon matrix might be too weak to interfere with the C 1*s* core electron binding energy.

The thermogravimetric analyses (TGA), performed under natural air, show a steep mass loss for GO at ≈150 °C, followed by a plateau, and finally total oxidation at 600 °C (**Figure 8**). Both rGO and rGO/Hg_{ads} have very similar behaviors both until 150 °C and for oxidation at 600 °C. The main difference is the 16% wt. mass loss from rGO/Hg_{ads} observed at ≈150 to 250 °C, which matches the range of the mass spectrometry peaks tracking both ^{200}Hg and ^{202}Hg. The release of mercury can be explained by the formation of HgO and subsequent decomposition into Hg° and O_2, which indeed has been observed at these relatively low temperatures on different solid substrates.[43]

Table 2. Deconvolution of the C 1*s* XPS peak for rGO and rGO/Hg_{ads}.

	Position [eV]	FWHM [eV]	Attribution	Contribution [%]
rGO	284.5	0.9	C sp2	49.7
	285.4	2.0	C sp3	32.4
	286.5	1.2	C—O	4.1
	287.7	1.8	C=O	3.7
	289.0	1.9	O—C=O	7.7
	291.1	1.9	π–π*	–
rGO/Hgads	284.5	0.9	C sp2	51.3
	285.4	2.0	C sp3	30.7
	286.5	1.0	C—O	2.9
	287.8	1.9	C=O	6.9
	289.2	2.0	O—C=O	5.6
	291.2	1.9	π–π*	–

Additionally, Fourier-transform infrared (FTIR) and Raman spectroscopies were applied to gain further information on the chemical composition and environment of the adsorbed mercury. In the FTIR spectra, recorded in the 750–3650 cm^{-1} range (Figure S10, Supporting Information), GO presents the characteristic fingerprints: a C=C vibrational mode at 1616 cm^{-1} and a strong peak at 1036 cm^{-1} related to the vibrational modes of —COOH groups.[44] Overall, both rGO and rGO/Hg_{ads} present very similar spectra, indicating little influence by the mercury, but the slight increase in the peak intensity for rGO/Hg_{ads} at around 1570 cm^{-1}, which is related to the aromatic ring, can be related to the presence of Hg, but this needs further verification.

It is, however, possible to confirm the reduction of GO to rGO, simply by the decreased intensity of the peaks related to the presence of oxygen-containing groups, such as carboxyl groups (—COOH) at 1036 and 1156 cm^{-1}. Furthermore, the shift of

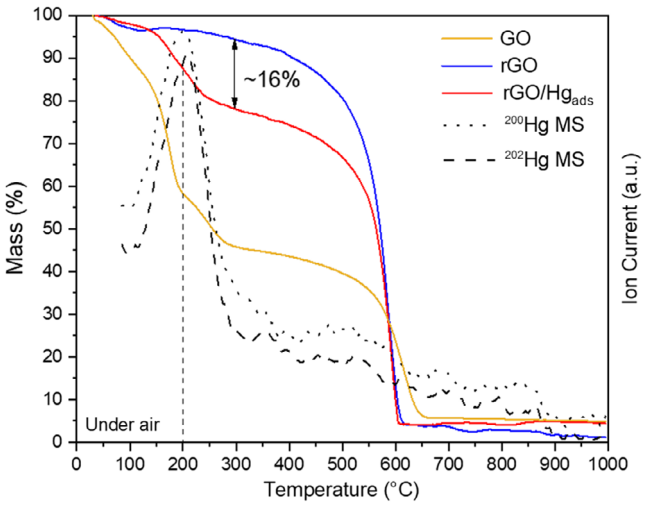

Figure 8. Thermogravimetric analysis under air flow for GO, rGO, and rGO/Hg_{ads} (straight lines) and mass spectrometry peaks for the rGO/Hg_{ads} experiment for ^{200}Hg and ^{202}Hg (dotted and dashed lines) evidencing the release of mercury at ≈200 °C.

the peak at 1616 cm^{-1} (GO, aromatic ring)[45] to 1564 cm^{-1} (rGO, aromatic ring)[46,47] indicates the removal of the oxygenated groups and the restructuring of the sp2 configuration.[44] The Raman spectroscopy data (Figure S11, Supporting Information) confirms the above analysis, but in addition, we can use five bands of rGO to gain more information. The D band indicates lattice defects, and the G band denotes in-plane sp2 carbon vibrations, and these are complemented by three less intense bands: the D′, D″, and D* bands, associated with intra-valley resonances, amorphous phases, and sp3 hybridization orbital structures, respectively.[48,49] The ratio between these intensities is detailed in Table S2, Supporting Information. The defect-related I_D/I_G ratio is 1.38 and 1.35 for GO and rGO, respectively, suggesting only minor changes in the concentration of defects by the GO to rGO reduction, while the I_G/I_D' ratio increased from 1.35 to 1.66, reflecting restoration of sp2 carbon networks. The defects are attributed to functional groups and the edges of graphene sheets, with the latter contributing more significantly to the slightly higher D band intensity.

2.3. Electrochemistry

The electrochemical behavior studies used an aqueous sulfuric acid electrolyte to explore the redox activity of the adsorbed mercury cations, together with the double-layer capacitance originating from the foam itself. The cyclic voltammograms (**Figure 9**a) show the rGO foam to exhibit a standard capacitive-like behavior, with a capacitance ranging from 200 to 250 F g^{-1} throughout the entire potential window, resulting in a maximum average capacity of 180 °C g^{-1} (per mass of total active material) within 0.8 V at 1 mV s^{-1}. The lower and upper cutoff potentials were selected according to the expected electroactivity region of the Hg^{2+} cations and the electrochemical stability windows of rGO and the electrolyte.

In the case of rGO/Hg_{ads}, the typical EDLC box-type-shaped envelope showed a similar behavior as rGO, that is, an average maximum capacitance of 200 F g^{-1} over a 0.8 V potential window, thus 160 C g^{-1}. The electroactivity of Hg^{2+} was evidenced by the appearance of sharp oxidation and reduction peaks centered at 0.62 V (0.65 and 0.59 V vs. SHE, respectively) associated to the proposed reversible electrochemical reaction (Reaction (8)). The peaks present less than 10 mV overpotential compared to the standard redox potential for this reaction, which can be due to the electrostatic stabilization of the mercury cations adsorbed at the surface of the carbon

$$2Hg^{2+}{}_{(aq)} + 2e^- \rightleftharpoons Hg_2{}^{2+}{}_{(aq)} \quad (E° = 0.63\,V \text{ vs. SHE}) \tag{8}$$

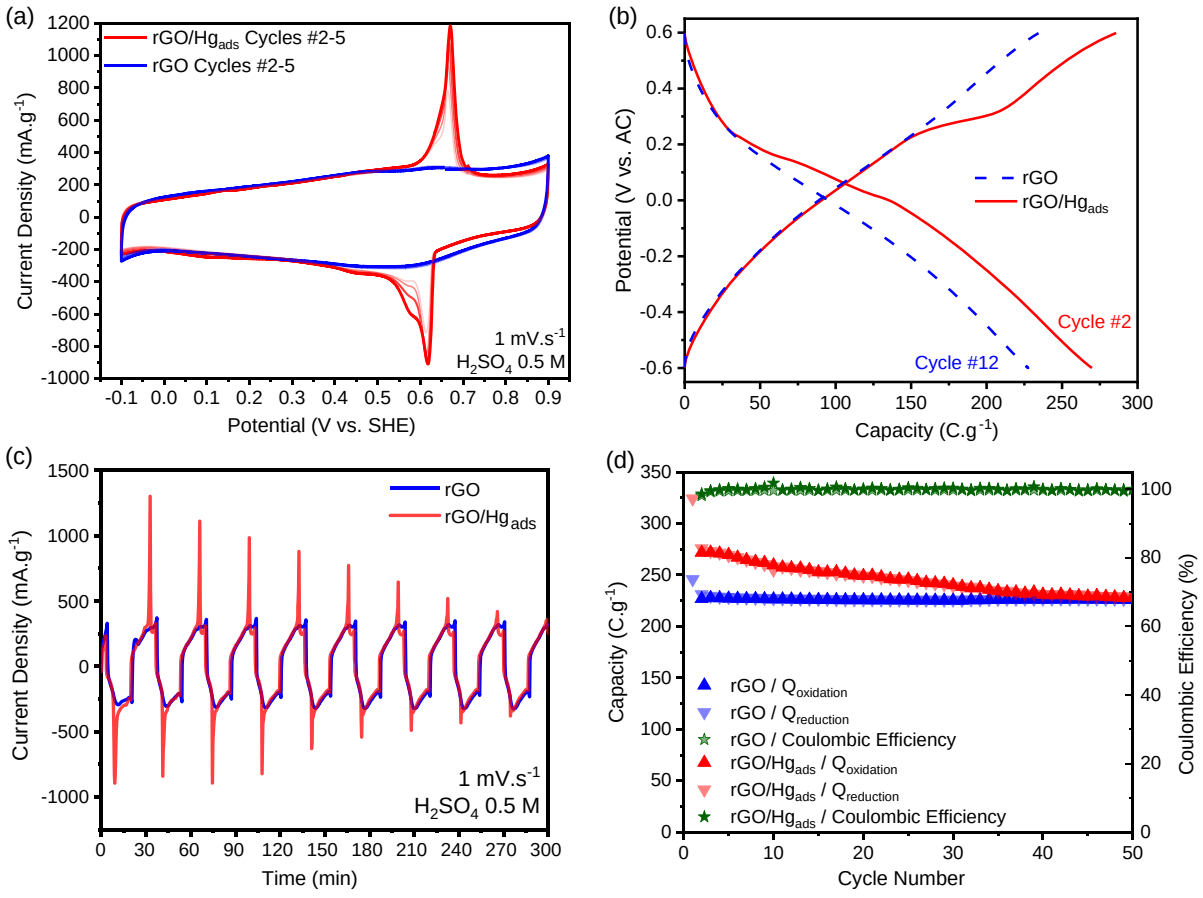

Figure 9. Electrochemical analyses of rGO (blue) and rGO/Hg_{ads} (red). a) Cyclic voltammetry—reference electrodes of Hg/Hg_2SO_4 in sat. K_2SO_4 reported versus SHE. b) Charge and discharge cycles at a constant current density of 0.2 A g^{-1}, c) Cyclic voltammetry current versus time. d) Capacity retention upon galvanostatic charge/discharge cycles with potential limitation (GCPL) cycling.

The as-prepared rGO/Hg_{ads} electrodes present an open circuit potential (OCP) about 50 mV higher than the redox potential shown in Reaction (8), which can be indicative of the presence of Hg^{2+} in the non-cycled rGO. The first CV cycle does not present any redox peaks; they appear after the second cycle when cycling a new cell from OCP in both oxidation and reduction directions (Figure S12, Supporting Information). This can be due to the reduction of Hg^{2+} into $Hg_2{}^{2+}$ species, which only then become reversibly electroactive. To reach a deeper understanding of the redox reaction, two rGO/Hg_{ads} electrodes with the exact same mass were left overnight immersed in (A) deionized (DI) water and (B) an H_2SO_4 0.5 M electrolyte, respectively. The cyclic voltammogram of the "A" treated electrode exhibits the sharp redox peaks associated to Reaction (8), just like the other freshly prepared cells with no resting time (Figure S13, Supporting Information). The "B" treated electrode, however, lacked the expected redox peaks, which tentatively can be explained by either the adsorbed mercury cations reacting with sulfuric acid, leading to the formation of $HgSO_4$ and therefore inhibiting Reaction (8), or by dissolution of the cations into the electrolyte.[37] The second hypothesis is supported by the cycling of rGO/Hg_{ads} in 1 M HNO_3 (Figure S14, Supporting Information), which initially presented the redox peaks, followed by their disappearance, which quite likely is due to the dissolution of the mercury cations into the acidic electrolyte, as this is how rGO adsorbents usually are recovered.[10,15,50]

By merging Equation (2)–(6) (Calculations Development **I** in the SI), the different contributions to the specific capacity (Q_{AM}, $C\,g^{-1}$) can be understood, and these are also correlated to the experimental data (q_{total}), as demonstrated in Figure S15, Supporting Information. Equation (9) is the assembled expression that correlates the specific capacity of the active material (Q_{AM}) as a function of the adsorbed mercury content (M%), describing the curves in Figure 2 and S15, whose parameters are summarized in Table S1, Supporting Information

$$Q_{AM} = \Delta V\left(C_{rGO} + \frac{C\%.C_{\text{conductive additive}}}{A\%}\right) + \left(\frac{nF}{M_w} - \Delta V.C_{rGO}\right)M\% \quad (9)$$

The cyclic voltammograms show the effective coupling between the capacitive contribution from carbon (double-layer capacitance) and the faradaic contribution coming from the presence of mercury redox activity. Overall, this finding makes this the first report of a heavy metal adsorbate that can be turned into an electrode for an energy storage device and, furthermore, for which the charge storage capacity can successfully be enhanced compared to the pristine adsorbent foam.

In detail, at the beginning of cycling, the charge and discharge cycles at a constant current density (0.2 A g^{-1}) show overlapping traces for rGO and rGO/Hg_{ads}. The capacity of rGO/Hg_{ads} then increases, and the curves separate, when they reach the potential at which mercury becomes electroactive (Figure 9b). This happens both for reduction and oxidation sweeps, in which the redox activity of the mercury cations is almost superimposed on the capacitive envelope of the rGO foam. The differences in capacity between rGO and rGO/Hg_{ads} during the 50 cycles arise from the adsorbed mercury's reversible redox behavior contributing to the electrode specific capacity during both oxidation and reduction reversibly. This process is evidenced by the increased maximum current of rGO/Hg_{ads} as compared to rGO, as shown in Figure 9c.

Furthermore, the adsorption of mercury leads to an increase in the density of the foam, hence, one of their recycled electrodes. Values of (0.72 ± 0.01) and (0.86 ± 0.03) g cm^{-3} were found for the rGO and rGO/Hg_{ads} electrodes, respectively. With this average 20% density increase, the volumetric capacity difference is even more significant between rGO and rGO/Hg_{ads} (Figure S15, Supporting Information), with 89.3 C cm^{-3} without mercury and 98.6 C cm^{-3} with mercury. In practice, the volumetric energy density is more appealing for potential applications of this technology, such as in stationary energy storage. The focus of this work in describing the fundamental electrochemical approach and mathematical description of this coupled system implies, however, the calculations in gravimetric units.

The galvanostatic cycling with potential limitation (GCPL) curves in Figure 9d show the capacity difference between rGO and rGO/Hg_{ads} from the beginning of the cycling, with the rGO capacity slightly increasing with time, while the rGO/Hg_{ads} capacity fades. This can (again, see above) be due to the progressive release of mercury cations into the electrolyte upon cycling, which ultimately leads to a similar capacity as the rGO after 40 cycles at 1 mV s^{-1} or 200 mA g^{-1}. Another hypothesis is the passivation of mercury into a non-electroactive form, such as the formation of $HgSO_4$. The phenomena are under fundamental investigation by, for example, *post-mortem* analysis, and among the mitigation strategies, we speculate both on altering the electrolyte composition and doing electrode surface engineering.

The GCPL data was further used to calculate the different charge contributions of the rGO/Hg_{ads} electrode using Equation (9) (Calculations Development II in the SI). The calculation using the second cycle capacity ($Q_{AM} = 272$ C g^{-1}, as compared to 231 C g^{-1} of rGO) indicates an equivalent $M\% = 14.5\%$ of mercury in the foam (Figure S15, Supporting Information), which is in strong agreement with the material characterization (≈16% wt. by both TGA and energy-dispersive X-ray (EDX)). Following up the calculation to cycle no. 50, the obtained capacity (228 C g^{-1}) results in a 6.0% electroactive mass of Hg, considering that m_{rGO} and C_{rGO} are constants throughout the cycling. If the capacity loss is purely associated with mercury release, that indicates that the remaining mercury is still electroactive, as confirmed by the CV by the appearance of new redox peaks associated with Reaction 3.

The initial increase in capacity of rGO can be explained by the progressive electrolyte access to the inner and smaller pores, taking into account the high tortuosity of the rGO foam microstructure.[51]

This effect can also be seen by the impedance decrease of the electrodes after cycling (Figure S17, Supporting Information): for rGO, from 11.2 to 6.1 Ω, and for rGO/Hg_{ads}, 42.9 to 9.1 Ω. The fact that rGO/Hg_{ads} presents the largest impedance drop is thus clearly not only related to the accessibility of the pores, as they are fewer as seen by BET, but also to the nonmetallic characteristics of the adsorbed species.

The power performance of the rGO/Hg_{ads} electrodes were tested with a sequence of cyclic voltammetry experiments (**Figure 10**). Coleman's model[52] was used to fit the experimental data according to Equation (10)

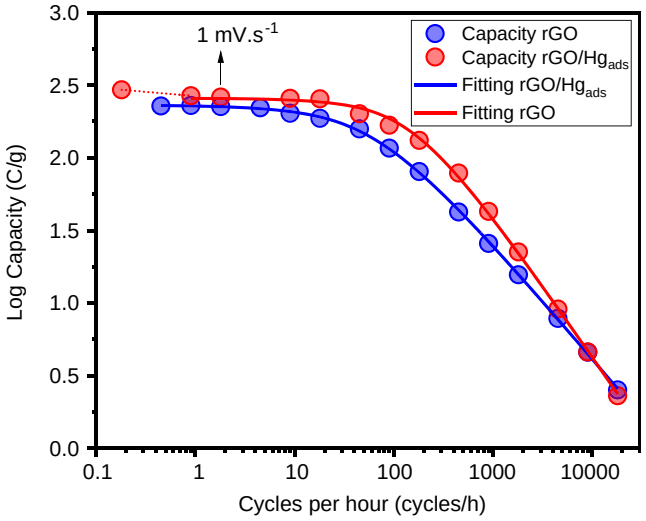

Figure 10. Power performance: Coleman plots of electrode capacities as a function of the scan rate. The cyclic voltammetry experiments ranged from 0.1 mV s^{-1} to 10 V s^{-1} in the potential range of −0.24 to 0.76 V (vs. Ag/AgCl). One electrode was used for the whole rGO experiment, while two different electrodes (cells) were required for the rGO/Hg_{ads} investigation, as the capacity fades quickly upon cycling. Capacity values were calculated by the integration of the reduction current (I [mA g^{-1}]) versus time (t [s]) curves on every third cycle at a given scan rate. The table shows the parameters derived from Coleman's equation (Equation (10)), where Q_{max} is the maximum capacity (C g^{-1}), τ is the time constant (s), and n is a constant related to the rate-limiting mechanisms.

$$\frac{Q}{M} = Q_M[1 - (R\tau)^n(1 - e^{-(R\tau)^{-n}})] \quad (10)$$

The rGO/Hg_{ads} outperformed the rGO foam at higher scan rates, presenting a time constant $\tau = 11.3$ s, half of that of the rGO, which is attributed to the fast mercury oxidation. Furthermore, both materials have an n (Coleman's exponent) close to 1, which indicates a resistance limitation, as expected for electrochemical capacitor materials.[52] As previously shown by both CV and GCPL, the rGO/Hg_{ads} has a higher capacity at lower scan rates, and at very slow cycling (0.1 mV s^{-1}), it presents a further gain in capacity, indicated by the red dashed line in Figure 10. Taken all together, the low value of the time constant τ and the electrochemical capacitor behavior at high scan rates are strong indications that the recycled adsorbent can be used in high-power devices and furthermore provide an extra capacity at lower scan rates, according to the demand, by effectively coupling faradaic and non-faradaic phenomena.

3. Experimental Section

3.1. Synthesis Procedures

3.1.1. Synthesis of Graphene Oxide (GO)

GO was synthesized starting from 3.0 g of graphite powder (TIMREX SFG6, S-154) *via* an improved Hummers' method. The graphite was added to 400 mL of a 9:1 mixture of sulfuric and phosphoric acids ($H_2SO_4 \geq 95\%$ Fisher; H_3PO_4 extra pure, 85% Thermo) in a 500 mL Erlenmeyer flask. After homogenization, the flask was placed in an ice bath, and 18 g of $KMnO_4$ (analytical grade, PROLABO) was slowly added under constant stirring. After equilibration, the ice bath was removed, and the mixture was continuously stirred at 50 °C for 3 h, followed by stirring at room temperature for 3 days. After that time, 400 mL of DI water was gradually added to the solution, followed by 5 mL of H_2O_2 (30% in water, Fisher) to consume the reminiscent permanganate. The solution was washed three times using 1% solution HCl (37% analytical grade, Fisher) and centrifugated at 5000 rpm for 15 min and three times with DI water with repeating cycles of centrifugation (10 000 rpm, 15 min) and discard of the supernatant. Finally, the slurry was sonicated for 1 h at 50 °C and centrifuged at 3500 rpm for 5 min with the collection of the supernatant, stored as a ≈10 mg mL^{-1} GO aqueous suspension.

3.1.2. Synthesis of Reduced Graphene Oxide (rGO)

The rGO foam was synthesized by diluting the GO suspension with DI water to 1 mg mL^{-1} and adding 35 mL into 50 mL Teflon liners. The reactors were heated to 180 °C for 12 h. After the cooling time, the self-standing rGO foam produced was thoroughly washed with DI water and frozen using liquid N_2 for the freeze-drying process.

3.2. Adsorption Experiments

3.2.1. Standard Heavy Metal Cations Solutions

A standard 1000 ppm solution of Hg (II) cations was prepared by dissolving 854 mg of $Hg(NO_3)_2.H_2O$ (> 98%, Thermo Scientific) in sufficient DI water up to a final volume of 500 mL, assuming 1 mg L^{-1} ≈ 1 mg kg^{-1} in the case of DI water. A similar procedure was used for the other studied cations, using $Pb(NO_3)_2$ (99%, Alfa Aesar), $Bi(NO_3)_3.5H_2O$ (98%, Alfa Aesar), and $Cr(NO_3)_3.9H_2O$ (98%, Alfa Aesar) salts. Other concentrations were achieved by appropriate dilutions with DI water.

3.2.2. Isothermal Adsorption

The adsorption experiments were performed by weighing around 10 mg of the dry rGO foam inside 25 mL glass vials. The foam was put under vacuum to properly impregnate the adsorbate solution using a Schlenk-like system, and 20 mL of the concentration-adjusted Hg^{2+} cations solution was introduced. The vials were added with a stir bar and left stirring in a temperature-controlled water bath for a determined amount of time. In the case of equilibrium time, t_{eq} was 150 min.

3.2.3. Concentration Analysis

To recover the foam after adsorption and evaluate the remaining Hg^{2+} cations concentration, the whole content of the vial was vacuum-filtered through a glass fiber filter paper (Whatman CAT no. 1823-070). The residue (rGO/Hg_{ads}) was taken for electrode preparation, and the filtrate was collected in a clean vial for

X-ray Fluorescence (XRF) analysis. The equipment (EDXRF Epsilon 1, Malvern Panalytical) was calibrated for mercury detection in aqueous solutions using a calibration curve (Figure S18, Supporting Information) with different known Hg^{2+} cation concentrations. The final remaining concentration and the adsorption capacity of the material were calculated in reference to the concentration of the blank experiment, in which the same procedure was followed (vacuum, temperature bath, filtration), but with no foam present.

3.3. Materials Characterization

3.3.1. Scanning Electron Microscopy and Energy-Dispersive X-ray Spectroscopy

SEM images were obtained using a Zeiss Merlin instrument at 15 kV. EDX analysis using a 50 mm^2 X-Max detector at a working distance of 8 mm was conducted on the same device using an OXFORD Instruments detector.

3.3.2. High-Resolution Scanning/Transmission Electronic Microscopy

HRSTEM was performed to locate the adsorbed mercury atoms in contrast to the carbon matrix. rGO and rGO/Hg_{ads} powders were dispersed in ethanol with the help of an ultrasonic bath and then deposited on a holey carbon film-coated copper grid before insertion in an aberration-corrected STEM Themis Z G3 (Thermo Fisher Scientific). High-angle annular dark-field (HAADF-STEM) images were acquired at 80 kV, with a 12.5 mrad convergence angle and 63–200 mrad collection angles. A Super-X system (four EDX detectors) was used to obtain the EDX spectra of the materials.

3.3.3. Thermogravimetric Analysis and Mass Spectrometry

TGA was performed under a constant airflow of 20 $cm^3\,min^{-1}$ from 30 to 1000 °C at 10 °C min^{-1} using an STA 449 F3 Jupiter NETZSCH instrument. Mass spectrometry was coupled to the TGA using a QMS 403 C Aëolos device.

3.3.4. X-ray Photoelectron Spectroscopy

The XPS measurements were performed on a Kratos Axis Nova using a monochromatic X-ray Al Kα source (1486.6 eV) at 20 mA and 15 kV. The surface analyzed was about 700 µm by 300 µm, and the instrument base pressure was 5×10^{-9} Torr. All samples were maintained on carbon conductive adhesive double tape. A pass energy (PE) of 80 eV was used to acquire wide-range survey spectra with a resolution of 0.9 eV for metallic silver. A PE of 40 eV was used to acquire narrow spectra of the C 1*s*, O 1*s*, and Hg 4*f* levels with a resolution of 0.55 eV measured on the Fermi edge of the valence band for metallic silver. Charge compensation has been used for every measurement. XPS data were analyzed using the CasaXPS software (version 2.3.24) using Gaussian/Lorentzian line shapes and Shirley background correction. All spectra were calibrated with hydrocarbon C 1*s* photoemission set to 285.0 eV binding energy.

3.3.5. BET

The carbon foams were characterized by gas sorption at liquid nitrogen temperature (77 K) using nitrogen gas with an ASAP 2020 Micromeritics equipment.

3.3.6. Raman Spectroscopy

Raman spectra were taken from 100 to 3800 cm^{-1}, using a resolution of ≈0.5 cm^{-1} and excitation by a 532 nm laser with a power $P = 1.5$ mW, in a S1800 device T64000 (Jobin Yvon).

3.3.7. Fourier-Transform Infrared Spectroscopy

FTIR spectroscopy was performed using a PerkinElmer instrument (Pike GladiATR) set to 1 cm^{-1} resolution and 12 scans.

3.4. Electrochemistry

3.4.1. Electrode Preparation

The recovered foam loaded with mercury cations (rGO/Hg_{ads}) was washed with DI water after filtration and frozen using liquid N_2 for freeze-drying overnight. As a comparative material, pure rGO foam was impregnated under vacuum with DI water, filtered, and freeze-dried under the same conditions. The electrode preparation followed the same procedure for both rGO and rGO/Hg_{ads} by mixing the active material with carbon black (PUREBLACK 205-110 Carbon Superior Graphite Co., Chicago, IL, USA) and a binder (PTFE 60% w/w aq. sol., Sigma-Aldrich) in the mass proportions 70:20:10, respectively. The powder mixture was dispersed with ethanol, and the slurry was stirred until the complete evaporation of the solvent. A self-standing film with a controlled thickness of about 100 µm was cold-rolled using a glass bar. Disk-shape self-standing electrodes were cut from the film using 10 mm punchers.

Thick activated carbon (AC) counter electrodes were prepared by mixing the active material (activated carbon YP50) with carbon black (PUREBLACK 205-110 Carbon Superior Graphite Co., Chicago, IL, USA) and a binder (PTFE 60% w/w aq. sol., Sigma-Aldrich) in the 85:10:5 mass proportions. The powders were dispersed with ethanol, mixed, and dried, and the final mixture was opened with a thickness of >1 mm to ensure a mass of the counter at least 15 times bigger than the working electrodes. The self-standing AC electrodes were cut with a diameter of 12 mm.

3.4.2. Cell Assembly

Swagelok-type cells were used for the electrochemical characterization. A three-electrode cell was assembled with the self-standing working electrode, two glass microfiber separators (1172-4113, Fisherbrand), and the counter electrode. The electrolyte (H_2SO_4 0.5 M, Fisher) was added in excess to wet the separators and cover the reference electrode (Ag/AgCl in 3 M NaCl or Hg/Hg_2SO_4 in sat. K_2SO_4), introduced on the third aperture of the cell (Figure S19, Supporting Information). A two-electrode cell configuration was used for the GCPL

experiments, using the thick AC electrodes as both counter and reference electrodes, as its potential was considered constant throughout the whole experiment, given its capacitance being more than 20 times bigger than that of the working electrode.

3.4.3. Measurements

Cyclic voltammetry and galvanostatic charge/discharge were performed using a VMP3 potentiostat (BioLogic, operated under EC-Lab software version V11.50) in an air-conditioned room (22 °C).

4. Conclusions

This study proposes a pioneering pathway for repurposing wastewater adsorbents into valuable materials for energy storage systems. It was demonstrated for the first time that recycling wastewater adsorbents as energy storage materials is a promising alternative to its treatment as solid waste. Using a single-step, one-pot-synthesized rGO foam, it was possible to effectively adsorb up to 240 mg g^{-1} of Hg^{2+} cations from water at 25 °C utilizing a material that is already known in both environmental sciences as a suitable adsorbent and in electrochemical energy storage as a performing electrode for electrochemical capacitors. Combining both properties and the existing demands on each field, a 15% specific capacity increase can be achieved by coupling the non-faradaic contribution of the carbon foam and taking advantage of the redox reactions of the loaded mercury cations, initially treated as waste. Moreover, the rGO adsorbent was used as prepared as an electrode material without the need for complex and/or costly additional processes.

Notably, further enhancing the cycling stability and capacity of the recycled materials is required to ensure their efficiency in practical applications. Furthermore, the development of such a device may involve different adsorbed cations. Indeed, a genuine choice of metal cations can provide two recycled electrodes with complementary potential windows that can be coupled to form a full cell configuration with both high capacity and efficiency. Despite these remaining challenges, our approach stands as a demonstration of the symbiotic potential between environmental remediation and energy storage technology. It is a proof of concept that applies a straightforward procedure to provide a second life to the solid toxic waste by recycling it as an active material for an electrochemical capacitor.

The use of recycled materials with direct application in energy storage is definitely underexplored in the literature. This research serves as a call to action for future work to bridge the existing gap between energy and environmental sciences, which must be filled with advanced, practical, accessible, and impactful scientific research. It advocates for a shift in focus toward utilizing readily available, recycled materials, which could be just as effective—if not more—than their complex and costly counterparts in energy storage applications. The pathway to advanced energy solutions may well be paved with the repurposing of what was once considered waste, pointing to a new era of innovation in material sciences within the framework of a circular economy.

Supporting Information

Supporting Information is available from the Wiley Online Library or from the author.

Acknowledgements

As a part of the DESTINY Ph.D. program, this publication is acknowledged by funding from the European Union's Horizon 2020 research and innovation program under the Marie Skłodowska-Curie Actions COFUND (grant agreement no. 945357). The authors are also grateful for the financial support from the Swedish Research Council (VR) Distinguished Professor grant "Next Generation Batteries" (no. 2021-00613). The authors would like to acknowledge the support of colleagues on the characterization by Eric Gautron (TEM/EELS), Jonathan Hamon (XPS), Barbara Daffos (BET), Camille Douard (electrochemistry and lab facilities), David Brown (TGA), and Thomas Fournier (SEM/EDS). Jonathan N. Coleman, Trinity College Dublin, is deeply acknowledged for providing the calculation tools for evaluating the power capability of the electrodes. This article was text-edited using the Open AI GPT-4o analysis tool, followed by careful revision and information checking by the authors.

Conflict of Interest

The authors declare no conflict of interest.

Author Contributions

Marcelo A Andrade: Formal analysis (lead); Investigation (lead); Methodology (lead); Visualization (lead); Writing—original draft (lead). **Olivier Crosnier**: Conceptualization (equal); Supervision (equal); Writing—review and editing (equal). **Patrik Johansson**: Validation (equal); Writing—review and editing (equal). **Thierry Brousse**: Conceptualization (lead); Project administration (lead); Supervision (lead); Writing—review and editing (equal).

Data Availability Statement

The data that support the findings of this study are available from the corresponding author upon reasonable request.

Keywords

mercury, recycling, RGO, supercapacitor, wastewater adsorbent

Received: July 26, 2024
Revised: August 5, 2024
Published online: September 2, 2024

[1] H. Ali, E. Khan, *Toxicol. Environ. Chem.* **2018**, *100*, 6.
[2] N. A. A. Qasem, R. H. Mohammed, D. U. Lawal, *npj Clean Water* **2021**, *4*, 36.
[3] M. C. Henriques, S. Loureiro, M. Fardilha, M. T. Herdeiro, *Reprod. Toxicol.* **2019**, *85*, 93.
[4] K. M. Rice, E. M. Walker, M. Wu, C. Gillette, E. R. Blough, *J. Prev. Med. Public Health* **2014**, *47*, 74.
[5] UN Environment, *Global Mercury Assessment 2018*, UN Environment Programme, Chemicals and Health Branch, Geneva, Switzerland **2019**.

[6] D. Q. Wang, X. X. Li, Z. J. Yang, T. Liu, G. D. Chai, G. Tang, X. Zheng, Y. S. Lin, *IOP Conf. Ser. Earth Environ. Sci.* **2019**, *344*, 012152.
[7] Regulation (EU) 2020/741, *Off. J. Eur. Union* **2020**, *177*, 32.
[8] Z. Othman, H. R. Mackey, K. A. Mahmoud, *Chemosphere* **2022**, *295*, 133849.
[9] D. Raj, S. K. Maiti, *Environ. Monit. Assess.* **2019**, *191*, 566.
[10] J. G. Yu, B. Y. Yue, X. W. Wu, Q. Liu, F. P. Jiao, X. Y. Jiang, X. Q. Chen, *Environ. Sci. Pollut. Res.* **2016**, *23*, 5056.
[11] R. Krishnamoorthy, B. Govindan, F. Banat, V. Sagadevan, M. Purushothaman, P. L. Show, *J. Biosci. Bioeng.* **2019**, *128*, 88.
[12] M. Melucci, V. Palermo, A. Kovtun, M. L. Navacchia, L. Bocchi, *EP3995457A1*, European Patent Office **2022**.
[13] L. P. Lingamdinne, S. K. Godlaveeti, G. K. R. Angaru, Y. Y. Chang, R. R. Nagireddy, A. R. Somala, J. R. Koduru, *Chemosphere* **2022**, *299*, 134457.
[14] C. Gao, Z. Dong, X. Hao, Y. Yao, S. Guo, *ACS Omega* **2020**, *5*, 9903.
[15] T. Tene, F. Arias, M. Guevara, A. Nuñez, L. Villamagua, C. Tapia, M. Pisarra, F. J. Torres, L. S. Caputi, C. Vacacela Gomez, *Sci. Rep.* **2022**, *12*, 6362.
[16] F. S. Awad, K. M. AbouZied, W. M. Abou El-Maaty, A. M. El-Wakil, M. S. El-Shall, *Arab. J. Chem.* **2020**, *13*, 2659.
[17] W. Wang, Z. Wang, J. Liu, Z. Zhang, L. Sun, *Sci. Rep.* **2017**, *7*, 9110.
[18] F. S. Awad, K. M. Abouzeid, W. M. A. El-Maaty, A. M. El-Wakil, M. S. El-Shall, *ACS Appl. Mater. Interfaces* **2017**, *9*, 34230.
[19] D. A. Gkika, A. C. Mitropoulos, G. Z. Kyzas, *Sci. Total Environ.* **2022**, *822*, 153612.
[20] Z. Chen, R. Zheng, W. Wei, W. Wei, W. Zou, J. Li, B. J. Ni, H. Chen, *Resour. Conserv. Recycl.* **2022**, *178*, 106037.
[21] J. B. Rial, M. L. Ferreira, *Sci. Total Environ.* **2022**, *823*, 153370.
[22] T. Velempini, M. E. H. Ahamed, K. Pillay, *Results Chem.* **2023**, *5*, 100901.
[23] C. B. Godiya, X. Cheng, D. Li, Z. Chen, X. Lu, *J. Hazard. Mater.* **2019**, *364*, 28.
[24] B. Verbinnen, C. Block, J. Van Caneghem, C. Vandecasteele, *Waste Manag.* **2015**, *45*, 407.
[25] T. Brousse, D. Bélanger, J. W. Long, *J. Electrochem. Soc.* **2015**, *162*, A5185.
[26] P. Simon, T. Brousse, F. Favier, in *Supercapacitors Based on Carbon or Pseudocapacitive Materials*, Wiley, London, UK **2017**.
[27] S. A. Bhat, V. Kumar, S. Kumar, A. E. Atabani, I. Anjum Badruddin, K. J. Chae, *Fuel* **2023**, *337*, 127125.
[28] P. Manasa, S. Sambasivam, F. Ran, *J. Energy Storage* **2022**, *54*, 105290.
[29] E. Lei, W. Li, C. Ma, Z. Xu, S. Liu, *Appl. Surf. Sci.* **2018**, *457*, 477.
[30] G. Li, Q. Li, J. Ye, G. Fu, J. J. Han, Y. Zhu, *J. Solid State Electrochem.* **2017**, *21*, 3169.
[31] S. Acharya, S. De, B. K. Mishra, G. C. Nayak, *J. Energy Storage* **2023**, *73*, 108938.
[32] Y. Wang, Y. Zhang, L. Pei, D. Ying, X. Xu, L. Zhao, J. Jia, X. Cao, *Sci. Rep.* **2017**, *7*, 41523.
[33] D. Pakulski, W. Czepa, S. Witomska, A. Aliprandi, P. Pawluć, V. Patroniak, A. Ciesielski, P. Samorì, *J. Mater. Chem. A* **2018**, *6*, 9384.
[34] P. Simon, Y. Gogotsi, *Nat. Mater.* **2020**, *19*, 1151.
[35] I. Shtepliuk, M. Vagin, R. Yakimova, *C—J. Carbon Res.* **2019**, *5*, 51.
[36] M. Kumar, J. S. Chung, S. H. Hur, *Appl. Sci.* **2019**, *9*, 2925.
[37] N. Takeno, *National Institute of Advanced Industrial Science and Technology*, Open File Report No. 419, Geological Survey of Japan **2005**.
[38] R. T. Myers, *Inorg. Chem.* **1974**, *13*, 2040.
[39] J. Biener, M. Stadermann, M. Suss, M. A. Worsley, M. M. Biener, K. A. Rose, T. F. Baumann, *Energy Environ. Sci.* **2011**, *4*, 656.
[40] CasaXPS, Help manual updates – XPS Spectra **2013**.
[41] R. D. Seals, R. Alexander, L. T. Taylor, J. G. Dillard, *Inorg. Chem.* **1973**, *12*, 2485.
[42] P. Humbert, *Solid State Commun.* **1986**, *60*, 21.
[43] M. Sedlar, M. Pavlin, A. Popovieč, M. Horvat, *Open Chem.* **2015**, *13*, 404.
[44] V. Ţucureanu, A. Matei, A. M. Avram, *Crit. Rev. Anal. Chem.* **2016**, *46*, 502.
[45] R. J. Seresht, M. Jahanshahi, A. Rashidi, A. A. Ghoreyshi, *J. Energy Environ.* **2013**, *4*, 53.
[46] S. Stankovich, R. D. Piner, S. B. T. Nguyen, R. S. Ruoff, *Carbon* **2006**, *44*, 3342.
[47] A. C. Obreja, D. Cristea, R. Gavrila, V. Schiopu, A. Dinescu, M. Danila, F. Comanescu, *Appl. Surf. Sci.* **2013**, *276*, 458.
[48] A. C. Ferrari, D. M. Basko, *Nat. Nanotechnol.* **2013**, *8*, 235.
[49] A. Y. Lee, K. Yang, N. D. Anh, C. Park, S. M. Lee, T. G. Lee, M. S. Jeong, *Appl. Surf. Sci.* **2021**, *536*, 147990.
[50] N. Ratner, D. Mandler, *Anal. Chem.* **2015**, *87*, 5148.
[51] M. Yaseen, M. A. K. Khattak, M. Humayun, M. Usman, S. S. Shah, S. Bibi, B. S. U. Hasnain, S. M. Ahmad, A. Khan, N. Shah, A. A. Tahir, H. Ullah, *Energies* **2021**, *14*, 7779.
[52] R. Tian, S. H. Park, P. J. King, G. Cunningham, J. Coelho, V. Nicolosi, J. N. Coleman, *Nat. Commun.* **2019**, *10*, 1933.